

Satellite galaxy abundance dependency on cosmology in Magneticum simulations

A. Ragagnin^{1,2,3}, A. Fumagalli^{2,3,4}, T. Castro^{2,3,4,5}, K. Dolag^{6,7}, A. Saro^{2,3,4,5}, M. Costanzi^{2,3,4}, S. Bocquet⁷

¹ Dipartimento di Fisica e Astronomia "Augusto Righi", Alma Mater Studiorum Università di Bologna, via Gobetti 93/2, I-40129 Bologna, Italy

e-mail: antonio.ragagnin@unibo.it

² INAF - Osservatorio Astronomico di Trieste, via G.B. Tiepolo 11, 34143 Trieste, Italy

³ IFPU - Institute for Fundamental Physics of the Universe, Via Beirut 2, 34014 Trieste, Italy

⁴ Astronomy Unit, Department of Physics, University of Trieste, via Tiepolo 11, I-34131 Trieste, Italy

⁵ INFN - National Institute for Nuclear Physics, Via Valerio 2, I-34127 Trieste, Italy

⁶ University Observatory Munich, Scheinerstr 1, D-81679 Munich, Germany

⁷ Max-Planck-Institut für Astrophysik (MPA), Karl-Schwarzschild Strasse 1, 85748 Garching bei München, Germany

submitted

ABSTRACT

Context. Modelling satellite galaxy abundance N_s in Galaxy Clusters (GCs) is a key element in modelling the Halo Occupation Distribution (HOD), which itself is a powerful tool to connect observational studies with numerical simulations.

Aims. To study the impact of cosmological parameters on satellite abundance both in cosmological simulations and in mock observations.

Methods. We build an emulator (HODEmu, <https://github.com/aragagnin/HODEmu/>) of satellite abundance based on cosmological parameters $\Omega_m, \Omega_b, \sigma_8, h_0$ and redshift z . We train our emulator using *Magneticum* hydrodynamic simulations that span 15 different cosmologies, each over 4 redshift slices between $0 < z < 0.5$, and for each setup we fit normalisation A , log-slope β and Gaussian fractional-scatter σ of the $N_s - M$ relation. The emulator is based on multi-variate output Gaussian Process Regression (GPR).

Results. We find that A and β depend on cosmological parameters, even if weakly, especially on Ω_m, Ω_b . This dependency can explain some discrepancies found in literature between satellite HOD of different cosmological simulations (Magneticum, Illustris, BAHAMAS). We also show that satellite abundance cosmology dependency differs between full-physics (FP) simulations, dark-matter only (DMO), and non-radiative simulations.

Conclusions. This work provides a preliminary calibration of the cosmological dependency of the satellite abundance of high mass halos, and we showed that modelling HOD with cosmological parameters is necessary to interpret satellite abundance, and we showed the importance of using FP simulations in modelling this dependency.

Key words. Galaxies: clusters: general – Cosmology: cosmological parameters – galaxies: abundances – methods: numerical

1. Introduction

Galaxy formation and evolution within a GC are connected to the properties of their underlying halo. This relationship, defined as the Galaxy-Halo (G-H) connection (see Wechsler & Tinker 2018, for a complete review on the topic and its applications) provides a powerful framework to test galaxy formation models (Reid et al. 2014; Coupon et al. 2015; Rodríguez-Puebla et al. 2017), to constrain cosmological parameters (Leauthaud et al. 2017), and as a proxy to calibrate halo masses (Zenteno et al. 2016).

One key topic in the G-H connection is the HOD (see Kravtsov et al. 2004, for a pioneering study on this topic), namely the conditional probability distribution $P(N|M)$ that a halo of mass M has a galaxy abundance N . In particular, HOD is widely used in the context of the Halo Model formalism (Peacock & Smith 2000; Cooray & Sheth 2002) which itself is used to predict Large Scale Structure (LSS) statistics (Murray et al. 2020).

The HOD is also particularly useful to calibrate cluster mass-proxies (Rozo et al. 2011), and thus to estimate the abundance

of galaxy clusters as a function of mass, which has long been recognised as a powerful cosmological tool (Peebles et al. 1989; Kokron et al. 2021), to connect galaxy properties to the evolution of dark matter haloes (Behroozi et al. 2013), to test abundance-matching techniques (Moster et al. 2010; Ronconi et al. 2020), to constrain the dynamical state of GCs (Zehavi et al. 2011; Zenteno et al. 2020), to produce mock catalogues of galaxies (Rossi et al. 2020; Zhai et al. 2021), and to model the halo mass function (Cueli et al. 2021). The HOD can be integrated with Semi Analytical Models (SAMs, Cole et al. 1994), providing a powerful tool to generate galaxy samples given their assembly history, for example (Angulo & Pontzen 2016; Croton et al. 2016; Jiang et al. 2021; Knebe et al. 2021).

In the context of HOD, galaxy counting is separated into central N_c and satellite N_s abundances so that:

$$N \equiv N_c + N_s. \quad (1)$$

In fact, central and satellite galaxies belong to two different populations as they experience different processes (Guzik & Seljak 2002) as shown by both observations (Skibba 2009) and numerical simulations (Wang et al. 2018): the satellite galaxy abun-

dance distribution $P(N_s|M)$ (i.e. the satellite HOD) is expected to follow a Poisson distribution at each mass bin (Kravtsov et al. 2004) and its average value should increase with halo mass; while the number of central galaxies N_c tends to unity asymptotically with respect to the galaxy mass selection threshold.

In this work, we limit our analysis to massive clusters, thus we will describe the full HOD with only the average satellite galaxy abundance $\langle N_s \rangle_M$ per mass bin.

Satellite abundance is typically computed within the virial radii R_{vir} (as in Kravtsov et al. 2004) or within R_{200c} (as in Devi et al. 2019), where these two radii encloses respectively the virial overdensity Δ_{vir} (see Bryan & Norman 1998) and 200 times the critical density of the Universe.

The average $N_s - M$ relation is known to follow a power law at high halo masses,

$$\langle N_s \rangle_M \propto M^\beta, \quad (2)$$

where normalisation should decrease with decreasing redshift. The log-slope β plays a key role in Galaxy Formation efficiency and it is not yet well constrained. Observations as Lin et al. (2004); Rines et al. (2004); Popesso et al. (2007); Zhai et al. (2017) found an exponent $\beta < 1$ which implies less galaxy formation efficiency for high-mass haloes (Hennig et al. 2017), while other studies point to an exponent > 1 (Zhou et al. 2021).

Results from numerical studies differ too: Anbajagane et al. (2020) found differences between $\langle N_s \rangle_M$ normalizations and slopes of various hydrodynamic cosmological simulation suites. This difference could be due to resolution as well as baryon physics implemented in the respective codes. In this study, we check whether these differences can be attributed to cosmological parameters.

Constraining the HOD is crucial for interpreting many observational studies (see e.g. Ross et al. 2010), and there are efforts to model HOD using additional halo properties besides mass: assembly bias (Hearin et al. 2016), the environment (Voivodic & Barreira 2020; Hadzhiyska et al. 2021b), a combination of them (Yuan et al. 2021), concentration (Avila et al. 2020), velocity dispersion (Hadzhiyska et al. 2021a). However most observational studies deal with a catalogue that have poor or no knowledge about their halo accretion histories (see e.g. Costanzi et al. 2019), and this motivates us to study the satellite HOD dependency only using cosmological parameters.

One may argue that a study on HOD cosmology dependency can be carried out using DMO simulations, which are in-expensive compared to FP simulations. However baryons are known to play a role inside galaxy clusters (Castro et al. 2021).

In this work, we will study the satellite abundance dependency on cosmological parameters based on hydrodynamic simulations. We build a GPR emulator of high-mass haloes satellite HOD and test the effect of a cosmology-dependent HOD on numerical study comparisons and mock observations. The emulator will be trained on results from the *Magneticum*¹ suite of hydrodynamic simulations (Biffi et al. 2013; Saro et al. 2014; Steinborn et al. 2015; Teklu et al. 2015; Dolag et al. 2015, 2016; Steinborn et al. 2016; Bocquet et al. 2016; Remus et al. 2017; Ragagnin et al. 2019). Here we employ a set of 15 runs with same initial conditions and run on different cosmological parameters (Singh et al. 2020; Ragagnin et al. 2021).

The paper is structured as follows: in Section 2 we describe in detail the numerical set up of the simulations used in this work. In Section 3 we fit the satellite abundance for all our simulations and snapshots we consider. In Section 4 we build an emu-

lator capable of predicting the high halo-mass regime of satellite HOD for a given cosmology and redshift. We devote Section 5 to comparing our emulator with other studies in the literature. We study the DMO vs. FP HOD impact on cosmology, and we study the effect of our emulator on mock observations. We draw our conclusions in Section 6.

2. *Magneticum* Simulations

Magneticum simulations are based on the N-body code P-Gadget3, which is an improved version of P-Gadget2 (Springel et al. 2005b; Springel 2005; Boylan-Kolchin et al. 2009), with a space-filling curve aware neighbour search (Ragagnin et al. 2016), and an improved Smoothed Particle Hydrodynamics (SPH) solver (Beck et al. 2016). These simulations include a treatment of radiative cooling, heating, ultraviolet (UV) background, star formation and stellar feedback processes as in Springel et al. (2005a) connected to a detailed chemical evolution and enrichment model as in Tornatore et al. (2007), which follows 11 chemical elements (H, He, C, N, O, Ne, Mg, Si, S, Ca, Fe) with the aid of CLOUDY photo-ionisation code (Ferland et al. 1998). Fabjan et al. (2010); Hirschmann et al. (2014) describe prescriptions for black hole growth and for feedback from AGNs.

Haloes together with their member galaxies are identified using respectively, the FoF halo finder (Davis et al. 1985) and an improved version of the subhalo finder SUBFIND (Springel et al. 2001), that takes into account the presence of baryons (Dolag et al. 2009).

In this work we mainly focus on a set of 15 simulations labelled Box1a/mr C1–C15 simulations. They span a range of $0.153 < \Omega_m < 0.428$, $0.0408 < \Omega_b < 0.0504$, $0.650 < \sigma_8 < 0.886$, $0.670 < h_0 < 0.732$, as presented in Tables 1 and 2, and are centered around the one of C8, that has WMAP7 cosmological parameters. For each simulation we study the haloes at a time slice with redshifts $z = 0.00, 0.14, 0.29, 0.47$.

In order to study resolution and mass-range of our emulator, we will use three additional *Magneticum* simulations, all with the same WMAP7 cosmology as C8: we use a high-resolution (HR) simulation Box2/hr² (Hirschmann et al. 2014); we use a ultra-high resolution simulation Box4/uh (Teklu et al. 2015) to study the emulator mass range validity on low-mass haloes; and a large-volume MR simulation (Box0/mr, Bocquet et al. 2016) in order to validate our satellite HOD results up to the most massive galaxy clusters of the Universe.

In this works, all masses and radius are expressed in physical units (unless in Table 1 where the units has been chosen differently for the sake of conciseness), thus they are not implicitly divided by $(1+z)$ or h_0 as other works on simulations.

3. Satellite HOD

To consistently compute and compare satellite HOD of our 15 simulations, in this section, we will first work out which stellar mass ranges provide a power-law regime for the $\langle N_s \rangle_M$ values (Sec. 3.1). Next, for every Box1a/mr simulation and redshift slice, we will fit a power-law relation that takes into account both the Poisson and a the Gaussian scatter of the abundance average (Sec. 3.2).

² Box2/hr haloes data is available in the web portal presented in Ragagnin et al. (2017)

¹ www.magneticum.org

Table 1. *Magneticum* simulations specifications used in this work: the Box0/mr, Box1a/mr, Box2/hr, and Box4/ubr. Columns from left to right present, the name, the cosmology (see Table 2), the box size in comoving Mpc/h, dark matter and initial gas particle masses m_{DM}, m_{gas} , and gravitational softening for dark matter, gas and stars $\epsilon_{DM}, \epsilon_{gas}, \epsilon_{stars}$.

Name	Cosmologies	Box size [aMpc/h]	m_{DM} $\left[M_{\odot}/h \frac{\Omega_m}{\Omega_{m,WMAP7}} \right]$	m_{gas} $\left[M_{\odot}/h \frac{\Omega_b}{\Omega_{b,WMAP7}} \right]$	ϵ_{DM} [akpc/h]	ϵ_{gas} [akpc/h]	ϵ_{stars} [akpc/h]
Box0/mr	C8	2688	$1.3 \cdot 10^{10}$	$2.6 \cdot 10^9$	10	10	5
Box1a/mr	C1-15	896	"	"	"	"	"
Box2/hr	C8	352	$6.9 \cdot 10^8$	$1.4 \cdot 10^8$	3.75	3.75	2
Box4/ubr	C8	48	$3.6 \cdot 10^7$	$7.3 \cdot 10^6$	1.4	1.4	0.7

Table 2. List of *Magneticum* cosmologies for the Box1a/mr C1–C15 simulations. Starred row (C8*) represents the original runs on WMAP7 cosmological parameters. Columns from left to right present, the name, cosmological parameters $\Omega_m, \Omega_b, \sigma_8, h_0$.

Name	Ω_m	Ω_b	σ_8	h_0
C1	0.153	0.0408	0.614	0.666
C2	0.189	0.0455	0.697	0.703
C3	0.200	0.0415	0.850	0.730
C4	0.204	0.0437	0.739	0.689
C5	0.222	0.0421	0.793	0.676
C6	0.232	0.0413	0.687	0.670
C7	0.268	0.0449	0.721	0.699
C8*	0.272	0.0456	0.809	0.704
C9	0.301	0.0460	0.824	0.707
C10	0.304	0.0504	0.886	0.740
C11	0.342	0.0462	0.834	0.708
C12	0.363	0.0490	0.884	0.729
C13	0.400	0.0485	0.650	0.675
C14	0.406	0.0466	0.867	0.712
C15	0.428	0.0492	0.830	0.732

3.1. Stellar mass cut

We now estimate which stellar mass cut to apply to the satellite count of our Box1a/mr C1–C15 simulations.

For this purpose we vary the stellar mass cut of both C8 and its HR counterpart (Box2/hr) until their $N_s - M$ relations statistically match. Figure 1 show convergence tests for stellar mass of C8 satellites. Left panel shows the $N_s - M$ relation of C8 and Box2/hr with the fiducial Box2/hr mass-cut $M_{\star} > 10^{10} M_{\odot}$ (as chosen in Anbajagane et al. 2020); central panel shows that a stellar mass cut $M_{\star} > 10^{11} M_{\odot}$ is not high enough to make C8 match its HR counterpart; right panel shows that a stellar mass cut $M_{\star} > 2 \cdot 10^{11} M_{\odot}$ is capable reconciling the two simulations.

We found that Box2/hr satellite HOD offset between its fiducial stellar mass cut ($10^{10} M_{\odot}$) and the C8 stellar mass cut ($2 \cdot 10^{11} M_{\odot}$) is

$$\frac{N_s(M_{\star} > 10^{10} M_{\odot})}{N_s(M_{\star} > 2 \cdot 10^{11} M_{\odot})} \approx 31, \quad (3)$$

for both Δ_{vir} and Δ_{200c} . We consider this number useful to compare emulated satellite abundance values (based on C1–C15 MR simulations) predictions together with HR simulations in literature with a cut $M_{\star} > 10^{10} M_{\odot}$.

To estimate the satellite count and compare it consistently between different cosmologies, one must choose a minimum stellar mass cut for each set of cosmological parameters. Following Anbajagane et al. (2020) we decided to re-scale the satellite stellar mass cut with $M_{\star} > 2 \cdot 10^{11} M_{\odot} \cdot f_b/f_{b,WMAP7}$.

From Figure 1 it is possible to see a drop in N_s in the low-mass end (in agreement with the drop at $M \ll M_{min}$ showed in Kravtsov et al. 2004, their Fig. 4). In order to keep the satellite HOD in the power-law regime we impose a C8 halo-mass cut of $M_{vir} > 3 \cdot 10^{14} M_{\odot}$ ($M_{200c} \approx 4.2 \cdot 10^{14} M_{\odot}$). We translated this cut to all Box1a/mr C1–C15 simulations by rescaling it according to their cosmological parameters, and, when necessary, enlarged or restricted the mass range by hand in order to maximise the power-law region (we present detail of all fits in Appendix A).

3.2. $N_s - M$ relation fit

We model the average satellite abundance as a power law as in Eq. 2, with a normalisation A and log-slope β as follows

$$\langle N_s \rangle_M = N_s(M, A, \beta) = A \cdot \left(\frac{M}{M_p} \right)^{\beta}, \quad (4)$$

where the pivot mass M_p is the median mass of the simulation with reference cosmology C8.

We fit A and β parameters by maximising a likelihood \mathcal{L} that models satellite HOD as the convolution of a Poisson and a truncated normal distribution defined in the range $x > 0$ with fractional scatter σ on the average satellite abundance, as follows

$$\mathcal{L}(A, \beta, \sigma) = \prod_i \frac{\int_0^{\infty} \mathcal{P}(N_{s,i}|n) \mathcal{N}(n|N_s(M_i, A, \beta), \sigma N_s(M_i, A, \beta)) dn}{\int_0^{\infty} \mathcal{N}(n|N_s(M_i, A, \beta), \sigma N_s(M_i, A, \beta))}, \quad (5)$$

where i runs over all haloes of a simulation snapshot.

We maximised³ the likelihood in Eq. 5 for all simulation separately and found that most fits have p -value ≈ 0.4 . We visually inspected some fits produced a p -value < 0.01 or p -value > 0.9 and found that they were performed on a very low number of resolved haloes and thus decided to remove them from further analyses. From the 15 simulations and 4 redshift slices we only managed to maximise Eq. 5 on 57 setups for $N_{s,vir}$ and 46 setups for $N_{s,200c}$ (see Appendix A for more details).

Figure 2 shows the power law fit for C8 and C15 at all available redshift (left panel) and for all simulations at $z = 0$ (right panel), where shaded area is the Gaussian scatter σ , showing that average satellite abundance differs on different cosmologies. We can qualitatively see that different cosmologies and redshift lead to different relations: log-slope can be below or above one depending mainly on Ω_m , and normalisation can vary up to a factor of two. We will quantify these dependencies in the next two subsections.

³ We used python package emcee from Foreman-Mackey et al. (2019)

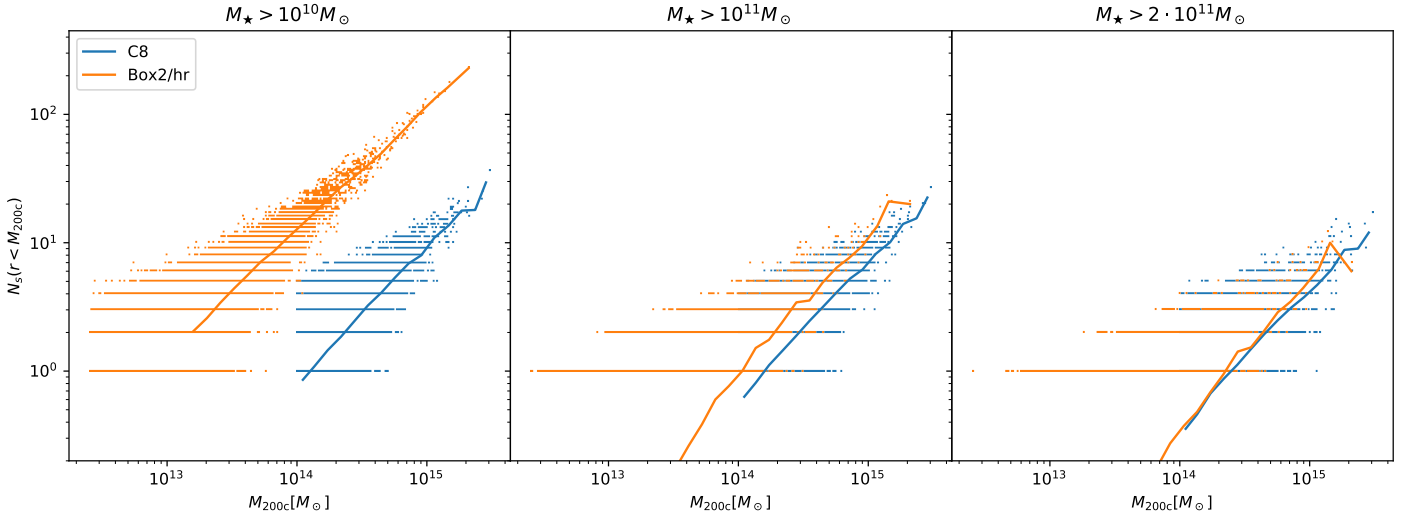


Fig. 1. Galaxy abundance of HR (Box2/hr in orange) and MR (C8 in blue) simulations for varying minimum stellar mass of galaxies: $M_* > 10^{10} M_\odot$ (left panel), $M_* > 10^{11} M_\odot$ (middle panel), an $M_* > 2 \cdot 10^{10} M_\odot$ (right panel).

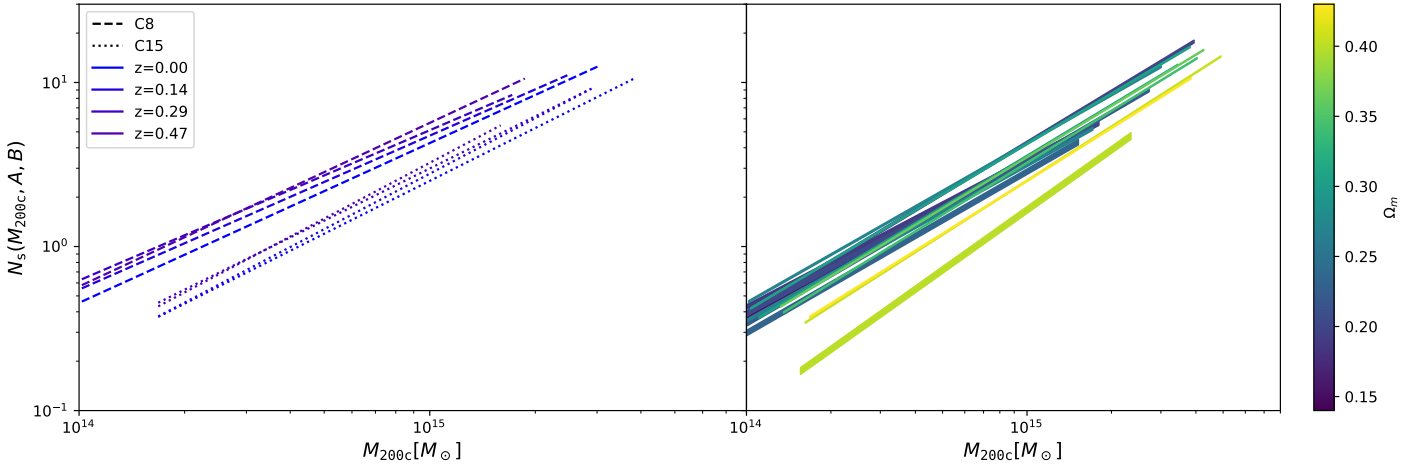


Fig. 2. Average satellite count within R_{200c} vs. halo mass for different simulations and redshifts as resulting from maximising Likelihood in Eq. 5. Left panel: relation for simulations Box1a/mr C8 (dashed lines) and C15(dotted lines) at 3 different redshifts (the redder the redshifted). Right panel: each line represents a simulation at $z = 0$, color coded with green with increasing Ω_m ; line tickness covers the gaussian scatter (poissonian scatter is omitted).

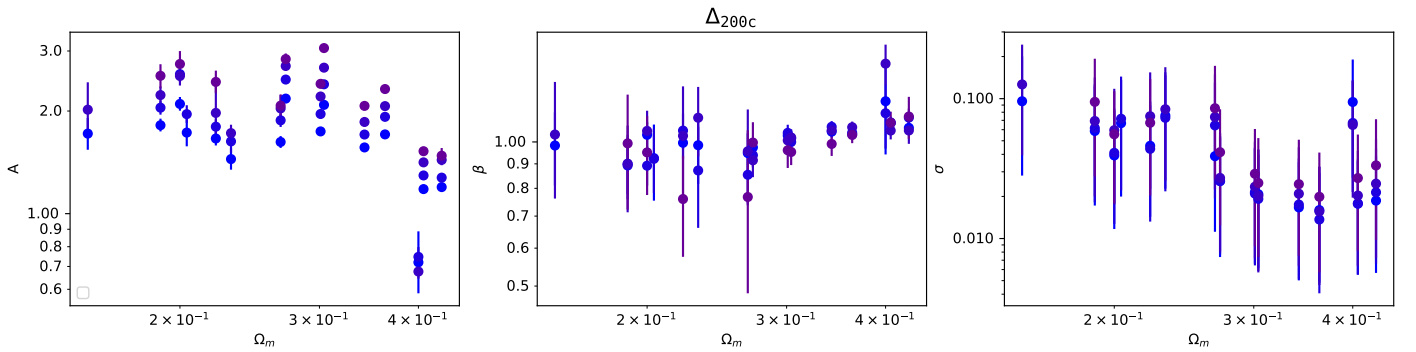


Fig. 3. Fit parameters of equations 5 and 4 for $N_{s,200c}$. From left to right, parameters A, B, σ as a function of Ω_m and colour-coded by $1 + z$ (the redder, the higher the red-shift). Vertical error bars corresponds to the uncertainty given from the Likelihood posterior in Eq. 5.

One may argue that the dependency from cosmological parameters on N_s is rooted on the fact that number of satellite depends on halo concentration and the halo concentration depends on cosmology. However, even if concentration and assembly bias play a role in the satellite count, it cannot account completely for the dependency between cosmological parameters shown in Fig.

2. In fact, Box1a/mr C13 simulation has an outstandingly low N_s normalisation, while it has not a particularly high concentration-mass normalisation (see Fig. 2 in Ragagnin et al. 2021).

In Figure 3 we summarise the parameters A, β , and σ found by maximising Eq. 5 for Δ_{200c} . Here we can see that normalisation A increases with redshift (in agreement with Kravtsov et al.

2004). The results that we found for overdensities Δ_{200c} and Δ_{vir} are very similar.

4. Satellite HOD Emulator

In order to model the HOD as a function of cosmological parameters and redshift, we build here an emulator based on GPR with the aim of predicting A, β, σ . Our main motivation is that the parameters do not follow simple functional forms as a power law (see Fig. 3).

For this purpose we train the GPR model⁴ on arrays of setups A_i, β_i, σ_i (where i runs on all setup) residuals with respect to a power-law fit on cosmological parameters. Here below we show fit results (we present fit posterior in Appendix B), for overdensity Δ_{vir} :

$$\begin{aligned} \ln(A_{\text{vir}}) &= 0.64_{-0.03}^{0.03} - 1.3_{-0.1}^{0.1} \ln\left(\frac{\Omega_m}{\Omega_{m,p}}\right) + 2.1_{-0.6}^{0.6} \ln\left(\frac{\Omega_b}{\Omega_{b,p}}\right) \\ &\quad + 2.5_{-0.3}^{0.3} \ln\left(\frac{\sigma_8}{\sigma_{8,p}}\right) - 0.8_{-0.1}^{0.1} \ln\left(\frac{a}{a_p}\right) \\ &\quad \pm 0.13 \\ \ln(\beta_{\text{vir}}) &= 0.01_{-0.01}^{0.01} + 0.29_{-0.07}^{0.06} \ln\left(\frac{\Omega_m}{\Omega_{m,p}}\right) - 0.7_{-0.3}^{0.3} \ln\left(\frac{\Omega_b}{\Omega_{b,p}}\right) \\ &\quad - 0.4_{-0.2}^{0.2} \ln\left(\frac{\sigma_8}{\sigma_{8,p}}\right) + 0.6_{-0.7}^{0.6} \ln\left(\frac{h_0}{h_{0,p}}\right) + 0.16_{-0.07}^{0.06} \ln\left(\frac{a}{a_p}\right) \\ &\quad \pm 0.069, \end{aligned} \quad (6)$$

and for overdensity Δ_{200c} :

$$\begin{aligned} \ln(A_{200c}) &= 0.65_{-0.03}^{0.03} - 1.3_{-0.1}^{0.1} \ln\left(\frac{\Omega_m}{\Omega_{m,p}}\right) + 1.9_{-0.7}^{0.6} \ln\left(\frac{\Omega_b}{\Omega_{b,p}}\right) \\ &\quad + 2.2_{-0.4}^{0.3} \ln\left(\frac{\sigma_8}{\sigma_{8,p}}\right) - 0.7_{-0.1}^{0.1} \ln\left(\frac{a}{a_p}\right) \\ &\quad \pm 0.13 \\ \ln(\beta_{200c}) &= 0.00_{-0.02}^{0.02} + 0.28_{-0.09}^{0.09} \ln\left(\frac{\Omega_m}{\Omega_{m,p}}\right) - 0.2_{-0.4}^{0.4} \ln\left(\frac{\Omega_b}{\Omega_{b,p}}\right) \\ &\quad - 0.3_{-0.2}^{0.2} \ln\left(\frac{\sigma_8}{\sigma_{8,p}}\right) + 0.1_{-0.8}^{0.9} \ln\left(\frac{h_0}{h_{0,p}}\right) + 0.09_{-0.08}^{0.08} \ln\left(\frac{a}{a_p}\right) \\ &\quad \pm 0.089. \end{aligned} \quad (7)$$

Pivot cosmology parameters are set to C8 values and pivot scale factor is $a = 0.87$. We removed h_0 dependency from the normalisation expression as it was consistent with zero. Being the log-scatter σ of Eq. 5 small and comparable with its own uncertainty ($\sigma \approx 0.04 \pm 0.03$), we do not report its fit results and we omit it from further analyses as this values, considering their large uncertainties, seem independent from cosmological parameters.

We trained our emulator on log-scaled values, as follows:

$$\begin{cases} X_i = \left[\ln\left(\frac{\Omega_{m,i}}{\Omega_{m,p}}\right), \ln\left(\frac{\Omega_{b,i}}{\Omega_{b,p}}\right), \ln\left(\frac{\sigma_{8,i}}{\sigma_{8,p}}\right), \ln\left(\frac{h_{0,i}}{h_{0,p}}\right), \ln\left(\frac{1+z_i}{1+z_p}\right) \right] \\ y_i = \left[\ln\left(\frac{A_i}{A_\Delta}\right), \ln\left(\frac{\beta_i}{\beta_\Delta}\right), \ln\left(\frac{\sigma_i}{\sigma_\Delta}\right) \right], \end{cases} \quad (8)$$

⁴ We used sklearn package (Pedregosa et al. 2011).

where $X = \{X_i\}$ is the input data, $y = \{y_i\}$ the output data; i runs over all data points (i.e. cosmology and snapshots) for which we maximised Likelihood in Eq. 5, and A_Δ, β_Δ and σ_Δ are a function of cosmology and, as pivot values, are the same as in Eq. 6 and Eq. 7. The overdensity Δ can be either 200c or vir.

Concerning the GPR model, we modelled our kernel K as a constant K_0 , times a gaussian Radial-basis function (RBF) kernel with length scale l :

$$K(\mathbf{x}_1, \mathbf{x}_2) = K_0 \times \exp\left(-\frac{\|\mathbf{x}_1 - \mathbf{x}_2\|^2}{2l^2}\right), \quad (9)$$

where the norm $\|\cdot\|$ is the euclidean distance.

We maximised the log marginal likelihood as proposed in Eq. 2.30 in Rasmussen & Williams (2005) and let parameters K_0 and l to vary in the maximisation.

Hereafter we define the Emulator predictions as $A^{\text{Emu}}, \beta^{\text{Emu}}$, which themselves depends on a cosmology and scale factor $(\Omega_m, \Omega_b, \sigma_8, h_0, a)$.

We define the emulated average number of satellites N_s^{Emu} as:

$$N_s^{\text{Emu}}(M, \text{cosmology}, z) = A^{\text{Emu}} \times \left(\frac{M}{M_p}\right)^{\beta^{\text{Emu}}}. \quad (10)$$

Fig. 4 left panel shows the number of satellite from *Magneticum* simulations. The right panel show the same number of satellites re-scaled to the C8 cosmology using the emulator predictions as follows:

$$N_{s,i} \mapsto N_{s,i} \times \frac{N_s^{\text{Emu}}(M_i, \text{C8}, z = 0.2)}{N_s^{\text{Emu}}(M_i, C_i, z_i)}, \quad (11)$$

where $N_{s,i}$ is the satellite abundance of a given halo, M_i, C_i, z_i its mass, cosmology and redshift and C8 is WMAP7 cosmology. As expected the mean satellite abundance of the re-scaled data set (orange band) does not overlap with the mean of the original sample (blue band): the emulator, re-scaling the number of satellite according to the cosmological models adopted and shifts the mean of the scaling relation.

In the next section we will see that the amplitude of this shift is sufficient to explain differences among satellite HOD studied in the literature.

4.1. Emulator error estimate

To estimate the precision of our emulator predictions we use the same technique as used by Bocquet et al. (2020): for each data vector available (X_i, y_i) , we (i) build a predictor trained on the complete data-set but that point (i.e. $[X, Y]_i = [\{X\} \setminus X_i, \{Y\} \setminus y_i]$), hereafter $O_{\text{Emu},i}$ and (ii) for each predictor we compute its relative error in predicting the un-trained value y_i .

To contextualise the relative error of the emulator, we will compare it with the relative error obtained by predicting y_i using only the average of all values (thus ignoring any cosmology dependency).

As we can see in Figure 5, the residual PDF of the emulators (orange steps) is much more peaked than the PDF from the predictor based on the averages (blue steps), implying that the emulator is indeed more effective in predicting satellite abundance than the simple average of A, β parameters.

The residuals distribution of the emulator within Δ_{vir} corresponds to a precision of 6% for A , 9% for β , while the average

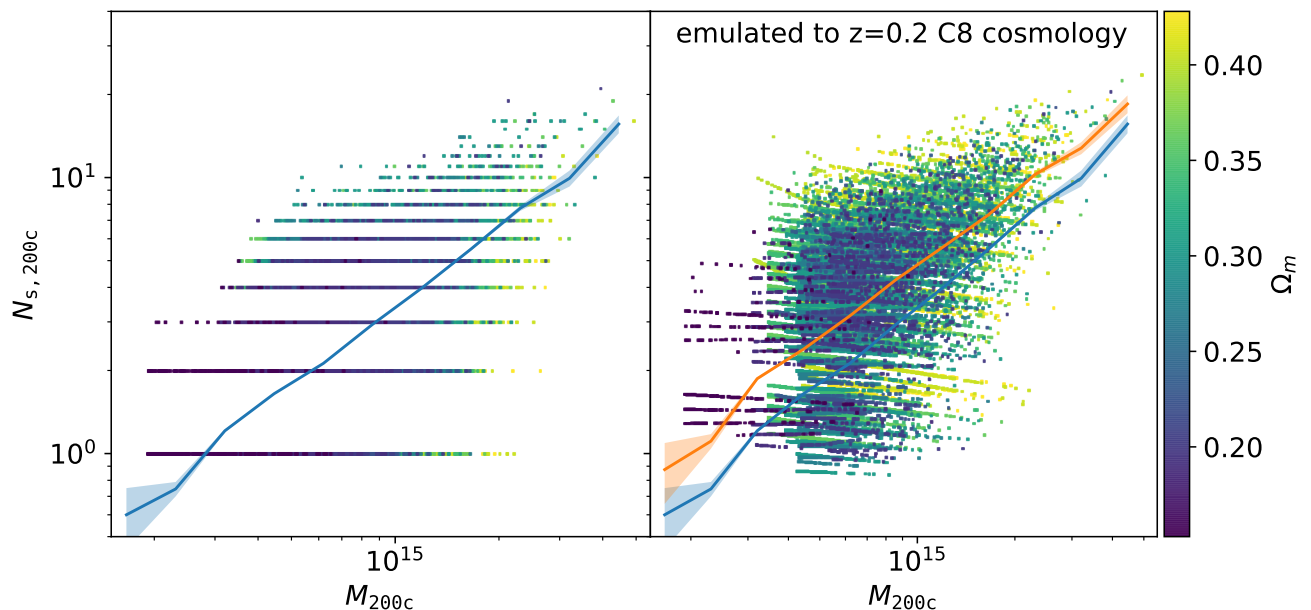


Fig. 4. Left panel: number of satellites as function of halo mass from the Box1a/mr C1–C15 simulations. Right panel: re-scaled with emulator according to Eq. 11. Average satellite abundance is traced by the blue (lower) line, the corresponding shaded area covers the error on the mean. The emulated average satellite abundance is traced by the orange upper line.

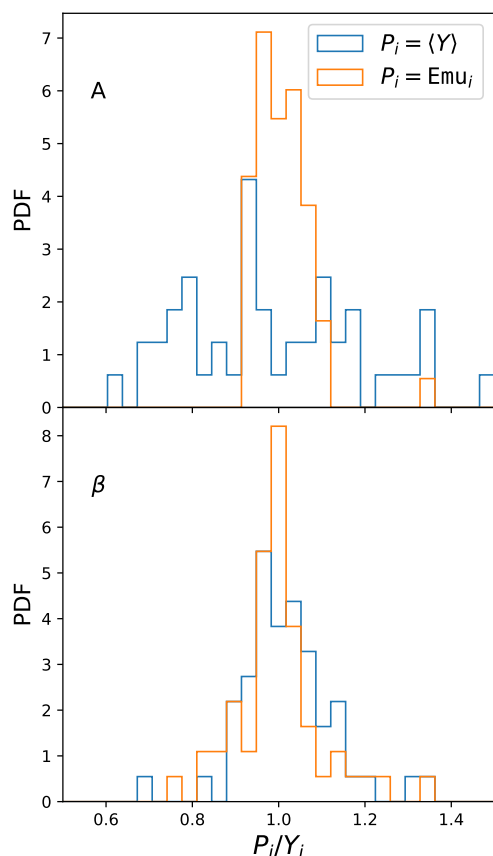


Fig. 5. PDF of residuals for predictor $P_i = \text{Emu}_i$ and the residual based on predictions from the average values ($P_i = \langle Y \rangle$), with respect to the missing data point y_i . Data is computed on overdensity Δ_{200c} . Upper row show PDF for $y_i = A_i$, lower row show PDF for $y_i = \beta_i$. The scatter obtained with the emulator is significantly smaller than the residuals on the averages

of the emulator error estimations in the missing points is, respectively 8% for A and 6% for β . The fact that the standard deviation of residuals and the emulator error estimation agree, implies that the emulator is capable of correctly predicting its own uncertainty.

For the Δ_{200c} emulator we computed a precision of 5% for A , 7% for β and 9% for σ .

5. Studies on cosmology dependent satellite HOD

In this section we employ the tools and results built in the previous section to study the impact of cosmology modelling of the satellite HOD. In particular, we use the emulator to compare results of other numerical studies, of mock catalogues, we study the emulator mass range and show the different impact of cosmological parameters on FP and DMO runs.

5.1. Comparison with numerical studies

Anbajagane et al. (2020) (see their Table 1 for more information) compared four hydrodynamic full-physics cosmological simulations: Illustris TNG 300 (Pillepich et al. 2018; Nelson et al. 2018; Springel et al. 2018; Marinacci et al. 2018), BAHAMAS 143Mpc (McCarthy et al. 2017), BAHAMAS+MACSIS (Barnes et al. 2017) and *Magneticum* Box2/hr (Hirschmann et al. 2014; Dolag et al. 2009) and found a difference between $\langle N_s \rangle_M$ normalisation and slopes (see their Figure 2). In particular their normalisation can differ of a factor 1.5, with BAHAMAS 143Mpc having the highest normalisation, *Magneticum* and BAHAMAS+MACSIS have similar slopes but different normalisation and Illustris has the highest log-slope and the only one that is steeper than unity. Up to now, the origin of these differences is not clear.

Since these simulations have all different cosmological parameters, in this subsection we use the Emulator to test if the

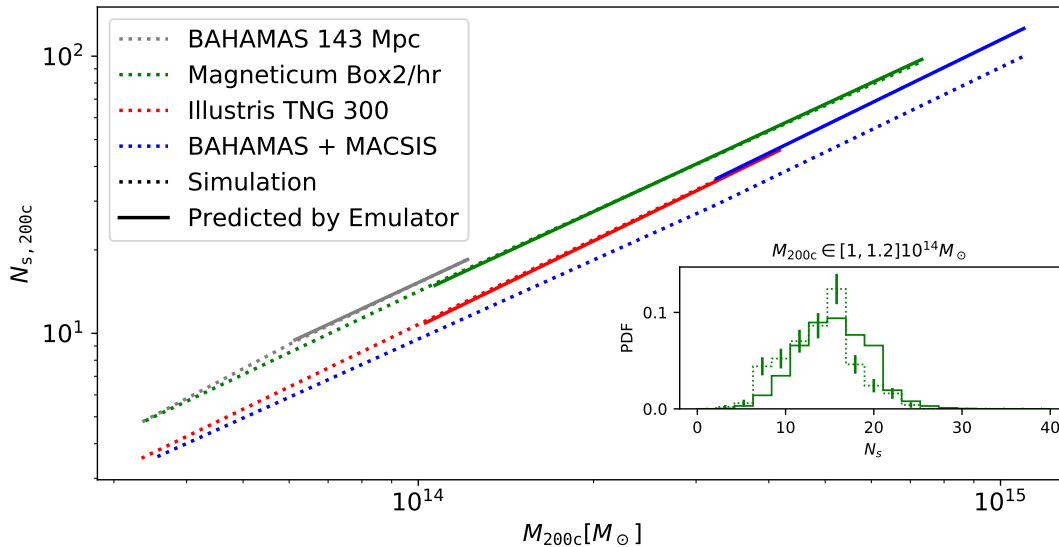


Fig. 6. Dotted lines show number of satellites as a function of halo mass as taken from Fig. 2 of Anbajagane et al. (2020) for simulations BAHAMAS high resolution (BM100, gray dashed line), *Magneticum* Box2b/hr (green dashed line), Illustris TNG 300 (red dashed line) and BAHAMAS+MACSIS (gray dashed line). Solid lines are the same cosmologies as predicted by our emulator rescaled with Eq. 3. Normalisation of dashed lines is ordered as in the legend. Inset shows the distribution of *Magneticum* Box2/hr satellites and the respective prediction from 100 realisations for each halo mass, both histogram refers to a mass range $10^{14} M_{\odot} < M_{200c} < 1.2 \cdot 10^{14} M_{\odot}$.

differences of satellite HODs of various simulations can be accounted, at least partially, by differences in their cosmological parameters.

In fact, BAHAMAS+MACSIS has parameters $\Omega_m = 0.3175$, $f_b = 0.154$, $\sigma_8 = 0.83$, BAHAMAS has parameters $\Omega_m = 0.279$, $f_b = 0.166$, $\sigma_8 = 0.82$ and a redshift $z \approx 0.1$, Illustris TNG 300 has parameters $\Omega_m = 0.31$, $f_b = 0.16$, $\sigma_8 = 0.82$, and MAGNETICUM has WMAP7 cosmological parameters. We do not report the difference in h_0 as the emulator has a very weak dependency on it and all simulations have a similar $h_0 \in [\approx 0.67, \approx 0.7]$.

Fig. 6 shows the N_s vs. halo mass of the four cosmological simulations and as predicted by our emulator at $z = 0$, when necessary, rescaled for the different stellar mass cut according to Eq. 3). We show the emulator prediction only for the high-mass power law regime.

The emulator is capable of predicting both slope and normalisation of Illustris and BAHAMAS 143 Mpc. On the other hand, the emulator over-predicts BAHAMAS+MACSIS normalisation. This discrepancy may be due to the fact that the emulator needs to be trained on more cosmologies or that MACSIS baryon physics description produces fewer satellites than *Magneticum*. For the *Magneticum* simulations, we also compare the satellite PDF with predictions from 100 realisations within the range of mass $10^{14} M_{\odot} < M_{200c} < 1.2 \cdot 10^{14} M_{\odot}$. (see inset plot in figure 6). The two PDFs agree on the peak position but the emulator predicts a symmetric distribution of N_s , while Box2/hr data points are skewed towards lower N_s values.

We now investigate the effect of each cosmological parameters on the $N_s - M$ relation. Figure 7 shows the parameters A_{Emu} , B_{Emu} variation from WMAP7 cosmology values, as a function of fractional variation of each cosmological parameter Ω_m , Ω_b , σ_8 , h_0 , a separately. We see almost no dependency on h_0 , (in agreement with the power law fit results in Eq. 6 and Eq. 7).

The normalisation decreases with Ω_m , which is in agreement with the low normalisation of Illustris, and decreases with scale factors, which is in agreement with the fact that BAHAMAS (that runs at $z = 0.1$) has a higher normalisation than *Magneticum*, yet it has very similar cosmological parameters.

The normalisation also increases with Ω_b . According to the emulator, this difference is causing Illustris low normalisation w.r.t. *Magneticum* (Illustris has $\Omega_b = 0.048$). The log-slope of the satellite HOD increases with Ω_m and explains why Illustris (that has higher Ω_m) has a high log-slope w.r.t. the other simulations.

5.2. Impact on mock observations

In this subsection we test the cosmology-dependence of the HOD on mock catalogues, in order to estimate the impact of such dependence on the cosmological parameter constraints. To this purpose, we consider the richness, a weighted sum of the galaxy members, often used as mass proxy in photometric cluster surveys. We recast Eq. 4 in terms of a richness-mass relation: 4 in the form of a richness-mass relation

$$\langle \lambda \rangle_M = A_{\lambda} \cdot \left(\frac{M}{M_p} \right)^{\beta_{\lambda}}, \quad (12)$$

with $A_{\lambda} = A_0 \cdot A_{\text{emu}} = 72.4 \pm 0.7$ and $\beta_{\lambda} = \beta_0 \cdot \beta_{\text{emu}} = 0.935 \pm 0.038$ (from table IV of Costanzi et al. 2021). Here, A_{emu} and β_{emu} are the predictions of the emulator and contain the dependence on cosmology, while A_0 and β_0 represent the cosmology-independent part of the total parameters.

To perform the analysis, we extract a catalogue of halo masses corresponding to the C8 simulation at redshift $z = 0$, following the Despali et al. (2016) analytical mass function. This step ensures to have a proper description of the mass function, in order to obtain an unbiased estimation of parameters. We obtain a catalogue with $\sim 2.8 \cdot 10^5$ objects, with virial masses above

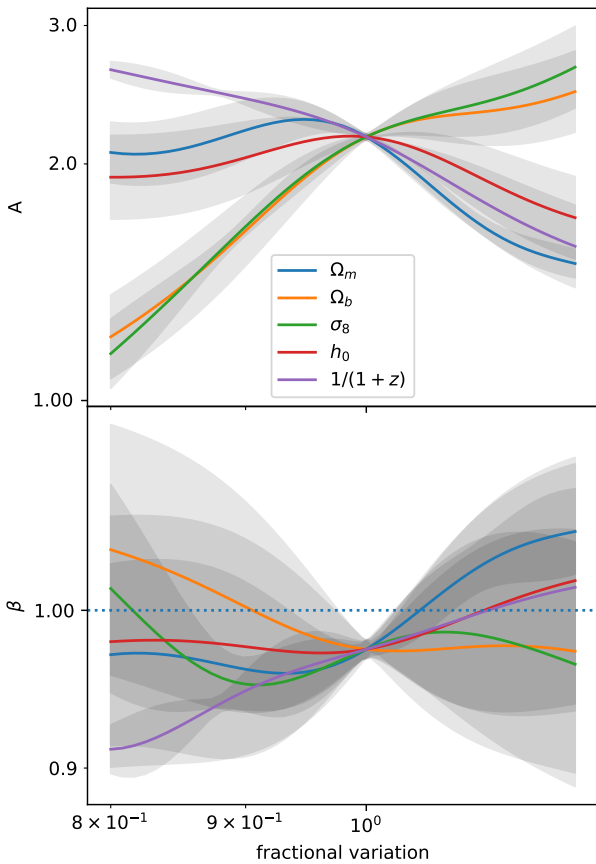


Fig. 7. Variation of $N_{s,200c}$ emulator A, β and σ as a function of fractional variation of cosmological parameters $\Omega_m, \Omega_b, \sigma_8, h_0$ and scale factor. Shaded areas show 1 standard deviation provided by the Gaussian Process error estimation.

$M_{\text{vir}} > 10^{13} M_{\odot}$, to which we assign richness by applying Eq. 12, plus a Poissonian scatter. To ease the analysis, we neglect the intrinsic scatter of the HOD, which is subdominant with respect to the Poissonian one. In the end, we compute the number counts by considering 5 richness bins, between $\lambda = 30 - 300$, where the sample is complete in mass.

Then, we compare the "observed" and analytical number counts distributions through a Gaussian likelihood

$$\mathcal{L}(x|\mu, C) = \frac{\exp\left\{-\frac{1}{2}(\mathbf{x} - \boldsymbol{\mu})^T C^{-1}(\mathbf{x} - \boldsymbol{\mu})\right\}}{\sqrt{2\pi \det C}}, \quad (13)$$

where \mathbf{x} and $\boldsymbol{\mu}$ are, respectively, the observed and analytical number counts and C is the covariance matrix, computed following the analytical model of Hu & Kravtsov (2003). Since in this test we only aim to give an estimation of the impact of the cosmology-dependent HOD, we run a simplified Monte Carlo Markov Chain (MCMC) process with only two free cosmological parameters, Ω_m and $\log_{10} A_s$ (and thus σ_8), neglecting the dependence of the HOD on Ω_b and h_0 , and neglecting the redshift dependence.

Following the approach of Singh et al. (2020), we compare three different cases:

- i *no cosmo* case: we ignore the cosmology dependence of the HOD, so that $A_{\lambda} = A_0$ and $\beta_{\lambda} = \beta_0$. We assume flat uninformative priors both on Ω_m and $\log_{10} A_s$ and on A_{λ} and β_{λ} ;
- ii *cosmo* case: we assume flat uninformative priors on Ω_m , $\log_{10} A_s$, A_0 and β_0 , plus Gaussian priors on A_{λ} and β_{λ} , respectively given by $\mathcal{N}(72.4, 7.0)$ and $\mathcal{N}(0.935, 0.038)$. The

cosmology-dependent parameters A_{emu} and β_{emu} are computed by the emulator at each step of the MCMC process, and, to take into account the emulator inaccuracy, we randomly extract a value from a Gaussian distribution with center in the emulator prediction and amplitude equal to

- iii *cosmo + WL* case: we add the weak lensing (WL) cosmological dependence which affects the mass calibration in the real observations, to figure out whether the combination of the cosmology-dependent HOD with other cosmological probes could improve the parameter constraints. We model such dependence by modifying the prior on A_{λ} , which becomes a Gaussian prior with the same amplitude of the previous case, but centered on

$$A'_{\lambda} = A_{\lambda} - \ln 10^{\Delta(\Omega_m)} \quad (14)$$

with $\Delta(\Omega_m) = \beta_{\lambda} \frac{d \ln M_{\text{WL}}}{d \Omega_m} (\Omega_m - 0.3)$, where $\frac{d \ln M_{\text{WL}}}{d \Omega_m} = -0.68$ is the average value from table I of Costanzi et al. (2019).

In Fig. 8 we show the posterior distributions resulting from the three analysis. As expected, the marginalised posteriors recovered by the *cosmo* case are similar to the ones from the *no cosmo* case, but in addition the former is able to constrain the cosmology-dependent and cosmology-independent components of the richness-mass relation separately. This can represent an advantage, since the components of A_{λ} show stronger degeneracies with cosmological parameters with respect to the one of their combination; such degeneracies can be exploited when combined with other cosmological probes. On the contrary, this decomposition for β_{λ} does not present the same advantage, as the full parameter has an higher degeneracy with cosmological parameters with respects to its components.

The third case presents similar posteriors to the simple *cosmo* case; to better compare the differences, we quantify the accuracy of the parameter estimation by computing the figure of merit (FoM, Albrecht et al. 2006)

$$\text{FoM}(\Omega_m, \sigma_8) = \frac{1}{\sqrt{\det C(\Omega_m, \sigma_8)}} \quad (15)$$

where $C(\Omega_m, \sigma_8)$ is the parameter covariance matrix obtained from the posteriors. The FoM is proportional to the inverse of the area enclosed by the ellipse representing the 68 percent confidence level: the higher the FoM, the more accurate is the parameter evaluation. The result, shown in table 3, indicates that the use of the cosmology-dependent HOD allows us to obtain more constraining posteriors, further improved with the addition of the weak lensing information. To prove that the *cosmo+WL* result is not achieved only thanks to the addition of WL, we show also the FoM for the *no cosmo + WL* case, which has a constraining power similar to the simple *no cosmo* case. By comparing the FoM of the three cases, we obtain an improvement of about the 6 percent for the *cosmo* case and of about the 11 percent for the *cosmo + WL* case with respect the *no cosmo* one.

5.3. Mass range of emulator

In this subsection we test the validity of our satellite HOD across various orders of magnitude in order to identify the halo mass range of it.

Figure 9 shows that the same power law satellite abundance holds from the most massive galaxy clusters $M_{200c} \approx 6 \cdot 10^{15} M_{\odot}$ down to haloes of $M_{200c} \approx 5 \cdot 10^{13} M_{\odot}$. At that mass there starts the low-mass drop of $M_{*} > 10^{10} M_{\odot}$ cut, which is particularly visible in the Box4/ubr regime haloes. Both Box0/mr and C8 satellite abundances are re-scaled using in Eq. 3.

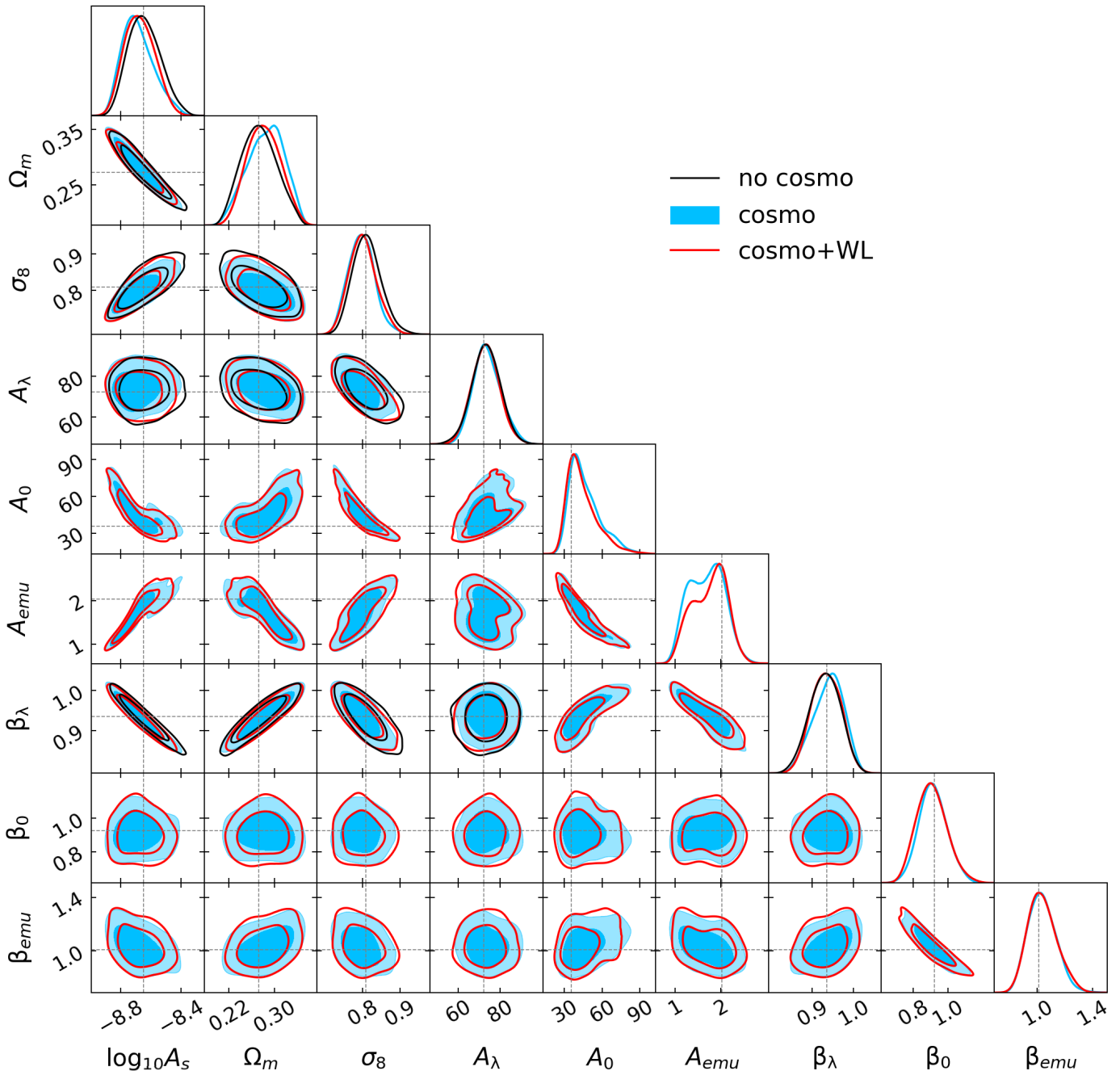


Fig. 8. Contour plots at 68 and 95 per cent of confidence level for the three cases described in Sect. 5.2: *no cosmo* (black), *cosmo* (blue) and *cosmo+WL* (red) contours. The grey dashed lines represent the input values of parameters.

Table 3. Figure of merit in the $\Omega_m - \sigma_8$ plane for the three cases of Fig. 8, plus the *no cosmo + WL* case. In the right column, normalised differences with respect to the *no cosmo* case.

Case	FoM	$\Delta\text{FoM}/\text{FoM}_{nc}$
no cosmo	980	-
no cosmo + WL	993	0.01
cosmo	1044	0.06
cosmo + WL	1088	0.11

5.4. Impact of cosmology on DMO–FP relations

In this subsection we demonstrate the need of considering full physics simulations in the context of satellite HOD calibration,

especially the fact that its cosmology dependency cannot be recovered from adiabatic runs (i.e. runs with no cooling and star formation, hereafter *norad*) or DMO simulations.

To this end, we first show that satellite HOD cannot be recovered in a DMO simulation using Subhalo abundance matching (SHAM) technique from a FP simulation that was run on a different cosmology. For this purpose we performed SHAM (with a stellar mass cut $M_\star > 2 \cdot 10^{11} M_\odot$) to C8 DMO both from its FP counterpart C8, and from C1. Figure 10 shows the resulting $N_s - M$ relations, and as expected SHAM from C8 to C8 DMO does match the original C8 FP average values. On the other hand, using C1 to perform SHAM on C8 DMO produces a too low satellite abundance.

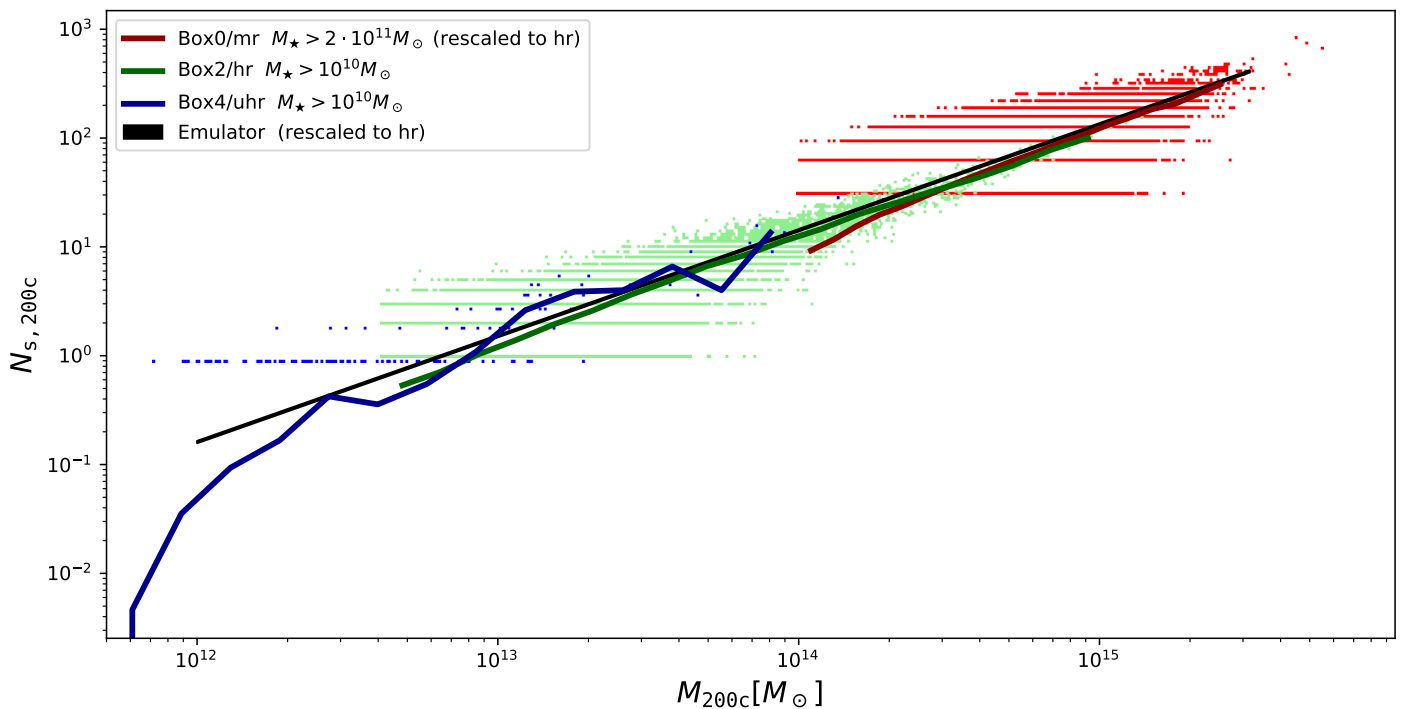


Fig. 9. Satellite count $N_{s,200c}$ vs. halo mass M_{200c} for three Magneticum simulations, Box4/uhr (blue coloured), Box2/hr (green coloured), and Box0/mr (red colour) to account for resolution effects. Data points represents single haloes, coloured lines represents average values per mass bin. Black line is emulator prediction. Emulator and Box0/mr data are re-scaled with Eq. 3.

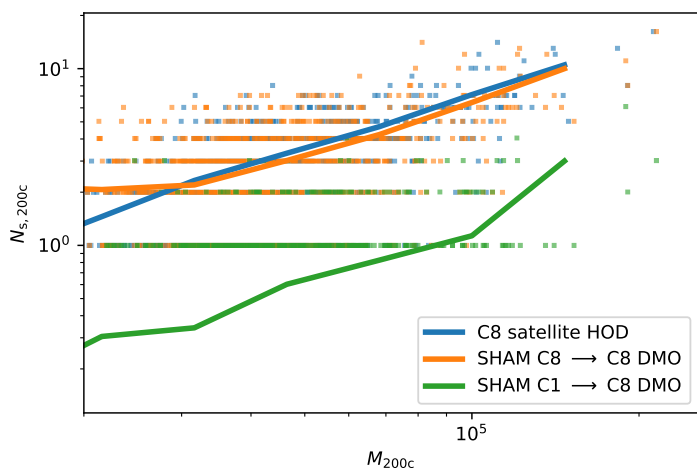


Fig. 10. Satellite count $N_{s,200c}$ vs. halo mass M_{200c} , respectively for C8 (blue coloured data), SHAM C8 DMO (orange coloured data), SHAM C8 DMO from C1 (green coloured data). Each data point represents a halo, solid lines represent the mean abundance per mass bin.

The reason of this mismatch lies in the fact that cosmological parameters have a different impact on sub-haloes evolution of DMO runs and galaxy evolution of FP runs.

To prove this statement, we compute $\langle N_s \rangle_M$ for two simulations of which we have the norad counterparts, Box1a/mr C1 and C15, and for two simulations of which we have the DMO counterpart, C8 and C1. Since DMO and non-radiative simulations have no stars, we count galaxy based on their total mass $M_{\text{GAL,tot}} > 10^{12} M_\odot$ which accounts for both baryons and DM and re-scaled with total matter cosmic fraction Ω_m .

Figure 11 shows the satellite abundance of these setups. Here we can see that C15 and its norad counterpart have almost the same satellite count, while C1 and its norad counterpart differ

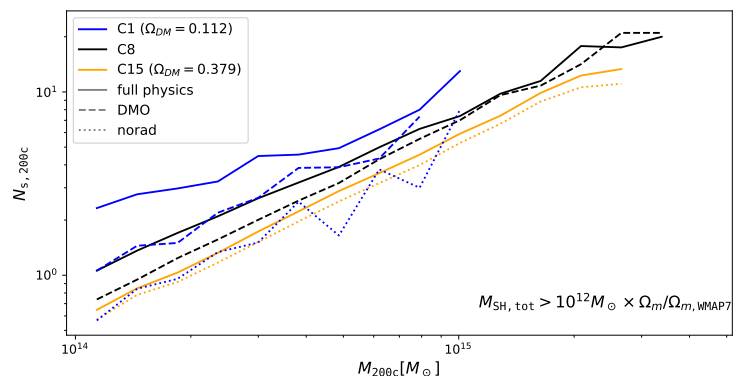


Fig. 11. Satellite count $N_{s,200c}$ vs. halo mass M_{200c} for Box1a/mr C1 (blue higher lower lines), C8 (black intermediate lines) and C15 (blue lower lines) simulations and their non-radiative (dotted lines, abbreviated with norad) counterpart and DMO counterparts (dashed lines) for galaxy masses $M_{\text{SH,tot}} > 10^{12} M_\odot \times \Omega_m / \Omega_{m,\text{WMAP7}}$.

of more than a factor of two. Additionally, the Ω_m rescaling in the subhalo mass cut is capable of matching C1 norad with C15 norad even if it has a ratio of ≈ 2.8 .

C1 and C8 have two different normalisation ratio with the respective DMO counterparts. Plus DMO HOD is systematically steeper than the respective FP run.

These two experiments shows that studying HOD dependency on non-FP simulations would have produced a different cosmology dependency than the one found in this work. On the other hand, once all major physical-phenomena are taken into account (i.e. cooling, star formation, SNe and AGN feedback), simulation suites tend to agree with each other on satellite HOD even if they implement different baryon physics models (as in Sec. 5.1).

6. Conclusions

We tackled the problem of studying the satellite count *vs.* halo mass relationship dependency on cosmological parameters and redshift and studied how this modelling affects comparison between current numerical simulations, mock observations and SHAM techniques. To this end we used 15 FP *Magneticum* simulations Box1 C1–C15 (see Table 1) that were run with the same initial conditions but different cosmological parameters $\Omega_m, \Omega_b, \sigma_8, h_0$. In particular:

- We showed that satellite abundance of *Magneticum* Box1a/mr C1–C15 simulations do depend on cosmological parameters.
- We built an emulator capable of predicting normalisation, log-slope and log-scatter of the high-mass power-law regime of the $N - M$ relation based on GPR modelling, in order to predict the number of satellites for a given cosmology. We made said emulator public (<https://github.com/aragagnin/HODEmu/>) and estimated its error being within $\approx 6 - 10\%$. This error is comparable with the same uncertainty predicted by the GPR, which ensures that the error estimation of the GPR is under control.
- The emulator shows that different satellite counts of cosmological simulations found in literature (*Magneticum*, *Illustris*, *BAHAMAS*) can be explained by their different cosmological parameters.
- The likelihood analysis on mock catalogues showed that the use of a cosmology-dependent HOD provides a slight improvement ($\sim 5\%$) in the constraining power over a simple cosmology-independent HOD, which can be further improved ($\sim 10\%$) if combined with multiple mass proxies, such as the weak lensing signal.
- We showed the importance of building an HOD emulator based on FP simulations (as opposed to DMO simulations) as its dependency on cosmological parameters is different with respect to full physics simulations.

The study was carried out over a small number of cosmologies and with a resolution limited to the high-mass regime of haloes.

The emulator log-slope predictions have a large uncertainty (see Figure 7 where β shaded area spans between $\beta \in [0.9, 1]$) which means there is the need for simulations over additional cosmological parameters in order to improve GPR interpolation.

Acknowledgements. The *Magneticum Pathfinder* simulations were partially performed at the Leibniz-Rechenzentrum with CPU time assigned to the Project ‘pr86re’. AF would like to thank Stefano Borgani for useful discussions. AR is supported by the EuroEXA project (grant no. 754337). KD acknowledges support by DAAD contract number 57396842. AR acknowledges support by MIUR-DAAD contract number 34843 ‘The Universe in a Box’. AS, AF and PS are supported by the ERC-StG ‘ClustersXCosmo’ grant agreement 716762. AS is supported by the the FARE-MIUR grant ‘ClustersXEuclid’ R165SBKTMA and INFN InDark Grant. This work was supported by the Deutsche Forschungsgemeinschaft (DFG, German Research Foundation) under Germany’s Excellence Strategy - EXC-2094 - 390783311. KD acknowledges funding for the COMPLEX project from the European Research Council (ERC) under the European Union’s Horizon 2020 research and innovation program grant agreement ERC-2019-AdG 860744. We are especially grateful for the support by M. Petkova through the Computational Center for Particle and Astrophysics (C²PAP). Information on the *Magneticum Pathfinder* project is available at <http://www.magneticum.org>.

References

Albrecht, A., Bernstein, G., Cahn, R., et al. 2006, *arXiv e-prints, astro*
Anbajagane, D., Evrard, A. E., Farahi, A., et al. 2020, *MNRAS*, **495**, 686

Angulo, R. E. & Pontzen, A. 2016, *MNRAS*, **462**, L1
Avila, S., Gonzalez-Perez, V., Mohammad, F. G., et al. 2020, *MNRAS*, **499**, 5486
Barnes, D. J., Kay, S. T., Henson, M. A., et al. 2017, *MNRAS*, **465**, 213
Beck, A. M., Murante, G., Arth, A., et al. 2016, *MNRAS*, **455**, 2110
Behroozi, P. S., Wechsler, R. H., & Conroy, C. 2013, *ApJ*, **770**, 57
Biffi, V., Dolag, K., & Böhringer, H. 2013, *MNRAS*, **428**, 1395
Bocquet, S., Heitmann, K., Habib, S., et al. 2020, *ApJ*, **901**, 5
Bocquet, S., Saro, A., Dolag, K., & Mohr, J. J. 2016, *MNRAS*, **456**, 2361
Boylan-Kolchin, M., Springel, V., White, S. D. M., Jenkins, A., & Lemson, G. 2009, *MNRAS*, **398**, 1150
Bryan, G. L. & Norman, M. L. 1998, *ApJ*, **495**, 80
Castro, T., Borgani, S., Dolag, K., et al. 2021, *MNRAS*, **500**, 2316
Cole, S., Aragon-Salamanca, A., Frenk, C. S., Navarro, J. F., & Zepf, S. E. 1994, *MNRAS*, **271**, 781
Cooray, A. & Sheth, R. 2002, *Phys. Rep.*, **372**, 1
Costanzi, M., Rozo, E., Simet, M., et al. 2019, *MNRAS*, **488**, 4779
Costanzi, M. et al. 2019, *Mon. Not. Roy. Astron. Soc.*, **488**, 488
Costanzi, M. et al. 2021, *Phys. Rev. D*, **103**, 103
Coupon, J., Arnouts, S., van Waerbeke, L., et al. 2015, *MNRAS*, **449**, 1352
Croton, D. J., Stevens, A. R. H., Tonini, C., et al. 2016, *ApJS*, **222**, 22
Cueli, M. M., Bonavera, L., González-Nuevo, J., & Lapi, A. 2021, *A&A*, **645**, A126
Davis, M., Efstathiou, G., Frenk, C. S., & White, S. D. M. 1985, *ApJ*, **292**, 371
Despali, G., Giocoli, C., Angulo, R. E., et al. 2016, *Mon. Not. Roy. Astron. Soc.*, **456**, 456
Devi, N. C., Rodríguez-Puebla, A., Valenzuela, O., et al. 2019, *MNRAS*, **488**, 782
Dolag, K., Borgani, S., Murante, G., & Springel, V. 2009, *MNRAS*, **399**, 497
Dolag, K., Gaensler, B. M., Beck, A. M., & Beck, M. C. 2015, *MNRAS*, **451**, 4277
Dolag, K., Komatsu, E., & Sunyaev, R. 2016, *MNRAS*, **463**, 1797
Fabjan, D., Borgani, S., Tornatore, L., et al. 2010, *MNRAS*, **401**, 1670
Ferland, G. J., Korista, K. T., Verner, D. A., et al. 1998, *PASP*, **110**, 761
Foreman-Mackey, D., Farr, W. M., Sinha, M., et al. 2019, emcee v3: A Python ensemble sampling toolkit for affine-invariant MCMC
Guzik, J. & Seljak, U. 2002, *MNRAS*, **335**, 311
Hadzhiyska, B., Bose, S., Eisenstein, D., & Hernquist, L. 2021a, *MNRAS*, **501**, 1603
Hadzhiyska, B., Tacchella, S., Bose, S., & Eisenstein, D. J. 2021b, *MNRAS*, **502**, 3599
Hearin, A. P., Zentner, A. R., van den Bosch, F. C., Campbell, D., & Tollerud, E. 2016, *MNRAS*, **460**, 2552
Hennig, C., Mohr, J. J., Zenteno, A., et al. 2017, *MNRAS*, **467**, 4015
Hirschmann, M., Dolag, K., Saro, A., et al. 2014, *MNRAS*, **442**, 2304
Hu, W. & Kravtsov, A. V. 2003, *Astrophys. J.*, **584**, 584
Jiang, F., Dekel, A., Freundlich, J., et al. 2021, *MNRAS*, **502**, 621
Knebe, A., Lopez-Cano, D., Avila, S., et al. 2021, *arXiv e-prints, arXiv:2103.13088*
Kokron, N., DeRose, J., Chen, S.-F., White, M., & Wechsler, R. H. 2021, *arXiv e-prints, arXiv:2101.11014*
Kravtsov, A. V., Berlind, A. A., Wechsler, R. H., et al. 2004, *ApJ*, **609**, 35
Leauthaud, A., Saito, S., Hilbert, S., et al. 2017, *MNRAS*, **467**, 3024
Lin, Y.-T., Mohr, J. J., & Stanford, S. A. 2004, *ApJ*, **610**, 745
Marinacci, F., Vogelsberger, M., Pakmor, R., et al. 2018, *MNRAS*, **480**, 5113
McCarthy, I. G., Schaye, J., Bird, S., & Le Brun, A. M. C. 2017, *MNRAS*, **465**, 2936
Moster, B. P., Somerville, R. S., Maubetsch, C., et al. 2010, *ApJ*, **710**, 903
Murray, S. G., Diemer, B., & Chen, Z. 2020, *arXiv e-prints, arXiv:2009.14066*
Nelson, D., Pillepich, A., Springel, V., et al. 2018, *MNRAS*, **475**, 624
Peacock, J. A. & Smith, R. E. 2000, *MNRAS*, **318**, 1144
Pedregosa, F., Varoquaux, G., Gramfort, A., et al. 2011, *Journal of Machine Learning Research*, **12**, 12
Peebles, P. J. E., Daly, R. A., & Juskiewicz, R. 1989, *ApJ*, **347**, 563
Pillepich, A., Nelson, D., Hernquist, L., et al. 2018, *MNRAS*, **475**, 648
Popesso, P., Biviano, A., Böhringer, H., & Romaniello, M. 2007, *A&A*, **464**, 451
Ragagnin, A., Dolag, K., Biffi, V., et al. 2017, *Astronomy and Computing*, **20**, 52
Ragagnin, A., Dolag, K., Moscardini, L., Biviano, A., & D’Onofrio, M. 2019, *MNRAS*, **486**, 4001
Ragagnin, A., Saro, A., Singh, P., & Dolag, K. 2021, *MNRAS*, **500**, 5056
Ragagnin, A., Tchipev, N., Bader, M., Dolag, K., & Hammer, N. J. 2016, in *Advances in Parallel Computing, Volume 27: Parallel Computing: On the Road to Exascale*, Edited by Gerhard R. Joubert, Hugh Leather, Mark Parsons, Frans Peters, Mark Sawyer. IOP Ebook, ISBN: 978-1-61499-621-7, pages 411-420
Rasmussen, C. E. & Williams, C. K. I. 2005, *Gaussian Processes for Machine Learning (Adaptive Computation and Machine Learning)* (The MIT Press)
Reid, B. A., Seo, H.-J., Leauthaud, A., Tinker, J. L., & White, M. 2014, *MNRAS*, **444**, 476
Remus, R.-S., Dolag, K., Naab, T., et al. 2017, *MNRAS*, **464**, 3742

- Rines, K., Geller, M. J., Diaferio, A., Kurtz, M. J., & Jarrett, T. H. 2004, *AJ*, **128**, 1078
- Rodríguez-Puebla, A., Primack, J. R., Avila-Reese, V., & Faber, S. M. 2017, *MNRAS*, **470**, 651
- Ronconi, T., Lapi, A., Viel, M., & Sartori, A. 2020, *MNRAS*, **498**, 2095
- Ross, A. J., Percival, W. J., & Brunner, R. J. 2010, *MNRAS*, **407**, 420
- Rossi, G., Choi, P. D., Moon, J., et al. 2020, *MNRAS* [arXiv:2007.09002]
- Rozo, E., Rykoff, E., Koester, B., et al. 2011, *ApJ*, **740**, 53
- Saro, A., Liu, J., Mohr, J. J., et al. 2014, *MNRAS*, **440**, 2610
- Singh, P., Saro, A., Costanzi, M., & Dolag, K. 2020, *MNRAS*, **494**, 3728
- Singh, P., Saro, A., Costanzi, M., & Dolag, K. 2020, *Mon. Not. Roy. Astron. Soc.*, **494**, 494
- Skibba, R. A. 2009, *MNRAS*, **392**, 1467
- Springel, V. 2005, *MNRAS*, **364**, 1105
- Springel, V., Di Matteo, T., & Hernquist, L. 2005a, *MNRAS*, **361**, 776
- Springel, V., Pakmor, R., Pillepich, A., et al. 2018, *MNRAS*, **475**, 676
- Springel, V., White, S. D. M., Jenkins, A., et al. 2005b, *Nature*, **435**, 629
- Springel, V., White, S. D. M., Tormen, G., & Kauffmann, G. 2001, *MNRAS*, **328**, 726
- Steinborn, L. K., Dolag, K., Comerford, J. M., et al. 2016, *MNRAS*, **458**, 1013
- Steinborn, L. K., Dolag, K., Hirschmann, M., Prieto, M. A., & Remus, R.-S. 2015, *MNRAS*, **448**, 1504
- Teklu, A. F., Remus, R.-S., Dolag, K., et al. 2015, *ApJ*, **812**, 29
- Tornatore, L., Borgani, S., Dolag, K., & Matteucci, F. 2007, *Monthly Notices of the Royal Astronomical Society*, **382**, 382
- Voivodic, R. & Barreira, A. 2020, *arXiv e-prints*, arXiv:2012.04637
- Wang, E., Wang, H., Mo, H., et al. 2018, *ApJ*, **864**, 51
- Wechsler, R. H. & Tinker, J. L. 2018, *ARA&A*, **56**, 435
- Yuan, S., Hadzhiyska, B., Bose, S., Eisenstein, D. J., & Guo, H. 2021, *MNRAS*, **502**, 3582
- Zehavi, I., Zheng, Z., Weinberg, D. H., et al. 2011, *ApJ*, **736**, 59
- Zenteno, A., Hernández-Lang, D., Klein, M., et al. 2020, *MNRAS*, **495**, 705
- Zenteno, A., Mohr, J. J., Desai, S., et al. 2016, *MNRAS*, **462**, 830
- Zhai, Z., Tinker, J. L., Hahn, C., et al. 2017, *ApJ*, **848**, 76
- Zhai, Z., Wang, Y., Benson, A., Chuang, C.-H., & Yepes, G. 2021, *arXiv e-prints*, arXiv:2103.11063
- Zhou, R., Newman, J. A., Mao, Y.-Y., et al. 2021, *MNRAS*, **501**, 3309

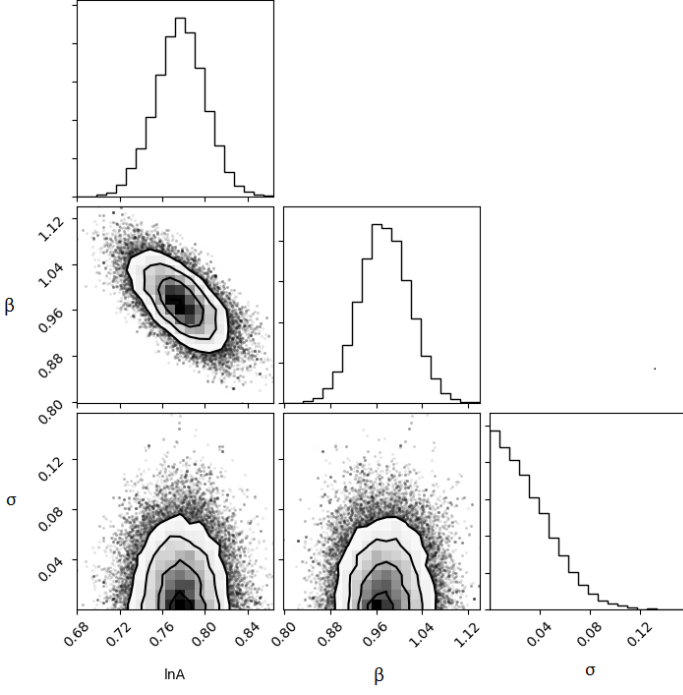


Fig. A.1. Posterior associated to Likelihood 5 for Box1a/mr C8 at $z = 0$ for $\Delta = 200c$. Parameters A and β are as in Eq. 4 and σ is the fractional-scatter in the Likelihood.

Appendix A: Satellite abundance fit for each simulation

Table A.1 reports the fit parameters of average satellite abundance a function of halo mass, for all setups that had a p -value below 0.9 and higher than 0.01. The problematic fits were the one at $z = 0.67$ where few of them failed, probably because the resolution of our simulations are not always enough to reach this redshift. Only a total of 48 fits were successful.

In order to fit the power-law halo-mass region of the satellite abundance relation, we imposed a halo mass cut (see Sec. 3.1) at $M_{\text{vir}} = 3 \cdot 10^{14} M_{\odot}$ for C8 simulation and scaled the mass cut to other simulations according to their baryon fraction. Some cuts have been modified in order to manually shrink or enlarge the halo range so to maximise the number of data points and yet do not cross the mass cut at low halo masses.

Figure A.1 shows the posterior of the fit for simulation Box1a/mr C8 $z = 0$. Here we can see that the fractional scatter σ is consistent with zero.

Appendix B: Cosmology dependent power-law fit posteriors

In this appendix we report detail results of A_{200c} fit. To fit this, and, similarly, also β and σ for both Δ_{200c} and Δ_{vir} (as in Eq. 6 and 7), we maximised a Likelihood as follows:

$$\ln \mathcal{L}(\ln A_0, e_{\theta}, \sigma) = -\frac{1}{2} \sum_i \left(\ln(2\pi\sigma^2) + \left(\frac{\ln A_{200c}(\ln A_0, e_{\theta}, C_i, z_i) - \ln A_{200c,i}}{\sigma} \right)^2 \right), \quad (\text{B.1})$$

where i runs over all setups, C_i and z_i are the cosmology and redshift of that setup, $A_{200c,i}$ is the normalisation found in Section 3 for a given setup (and presented in Fig. ??), e_{θ} is a set of

exponents ($e_m, e_b, e_{\sigma}, e_h, e_a$) for the respective input parameters $\theta_i = (C_i, a_i) = (\Omega_{m,i}, \Omega_{b,i}, \sigma_{8,i}, h_{0,i}, a_i)$, and σ is the fractional scatter, and A_{200c} has a power-law dependency from cosmological parameters, as follow

$$\ln A_{200c}(\ln A_0, e_{\theta}, \theta_i) = \ln A_0 + \sum_i e_i \ln \frac{\theta_i}{\theta_{i,p}}, \quad (\text{B.2})$$

where the pivot values $\theta_{i,p}$ are presented in Sec. 4. Figure B.1 shows an example of posterior distribution of parameters ($\ln A_0, e_{\theta}, \sigma$) for a single snapshot.

The evaluation of $\beta_{200c}, \sigma_{200c}, A_{\text{vir}}, \beta_{\text{vir}}$ and σ_{200c} have been performed in the same way as described above.

Table A.1. Each row presents data for a given cosmology C1–C15 of Box1a/mr simulations, columns are grouped by redshift slices, and each redshift slice reports the halo mass cut M_{cut} in units of $10^{14} M_{\odot}$ and the corresponding parameters A , B and σ of Eq. 4. Upper rows present data for overdensity Δ_{vir} and lower rows for overdensity 200c.

	$z = 0.00$				$z = 0.14$				$z = 0.29$				$z = 0.47$			
	M_{cut}	$\ln A$	β	σ	M_{cut}	$\ln A$	β	σ	M_{cut}	$\ln A$	β	σ	M_{cut}	$\ln A$	β	σ
$\Delta = \text{vir}$																
C1	2.9	0.43	1.00	0.11	-	-	-	-	-	-	-	-	-	-	-	-
C2	3.3	0.49	1.01	0.05	4.0	0.60	1.02	0.05	3.3	0.69	0.90	0.06	3.3	0.85	0.88	0.09
C3	5.7	0.68	1.04	0.03	5.7	0.82	1.02	0.03	5.7	0.95	0.96	0.04	5.7	0.90	1.06	0.05
C4	4.1	0.48	0.97	0.03	5.9	0.63	0.85	0.06	-	-	-	-	-	-	-	-
C5	5.2	0.38	1.05	0.03	5.2	0.51	1.05	0.04	7.8	0.59	1.06	0.08	5.2	0.81	0.86	0.07
C6	3.9	0.23	1.04	0.05	4.9	0.34	1.05	0.06	3.9	0.36	1.23	0.07	-	-	-	-
C7	4.6	0.37	1.03	0.03	4.6	0.50	1.01	0.04	5.5	0.62	0.97	0.06	4.6	0.70	0.88	0.08
C8	4.6	0.71	1.01	0.02	4.6	0.82	0.99	0.02	4.6	0.91	0.96	0.03	4.6	1.01	0.93	0.04
C9	4.2	0.51	1.03	0.02	4.2	0.59	1.06	0.02	8.4	0.76	0.97	0.04	4.2	0.81	1.01	0.03
C10	4.5	0.70	1.03	0.02	4.6	0.83	1.01	0.02	4.6	0.94	1.01	0.02	4.6	1.06	1.00	0.02
C11	3.7	0.37	1.08	0.01	3.7	0.46	1.08	0.02	3.7	0.56	1.07	0.02	3.7	0.67	1.01	0.02
C12	5.6	0.51	1.03	0.02	5.6	0.62	1.03	0.02	5.6	0.70	1.04	0.02	5.6	0.79	1.04	0.03
C13	10.0	-0.57	1.34	0.08	5.0	-0.43	1.20	0.06	5.0	-0.39	1.16	0.08	-	-	-	-
C14	4.7	0.09	1.11	0.02	4.7	0.18	1.10	0.02	4.7	0.28	1.06	0.02	4.7	0.38	1.07	0.03
C15	5.7	0.10	1.08	0.02	5.7	0.16	1.15	0.02	5.7	0.29	1.08	0.02	5.7	0.34	1.14	0.04
$\Delta = 200c$																
C1	1.9	0.54	0.98	0.10	-	-	-	-	-	-	-	-	-	-	-	-
C2	3.1	0.60	0.90	0.06	3.1	0.72	0.89	0.06	3.1	0.80	0.90	0.07	3.1	0.93	0.99	0.09
C3	5.3	0.74	1.03	0.04	5.3	0.94	0.89	0.04	5.4	0.93	1.05	0.06	5.3	1.01	0.95	0.06
C4	5.5	0.55	0.93	0.07	4.4	0.67	0.92	0.07	-	-	-	-	-	-	-	-
C5	4.9	0.51	1.00	0.05	4.9	0.59	1.06	0.04	7.3	0.68	1.03	0.07	4.9	0.89	0.76	0.07
C6	4.6	0.37	0.98	0.08	4.6	0.49	0.87	0.07	3.7	0.54	1.12	0.08	-	-	-	-
C7	4.3	0.48	0.95	0.04	4.3	0.63	0.85	0.06	5.2	0.71	0.96	0.07	4.3	0.73	0.77	0.09
C8	4.3	0.78	0.97	0.03	4.3	0.91	0.94	0.03	4.3	1.00	0.92	0.03	4.3	1.04	1.00	0.04
C9	3.9	0.56	1.03	0.02	3.9	0.67	1.04	0.02	3.9	0.79	1.01	0.02	3.9	0.88	0.96	0.03
C10	4.2	0.73	1.02	0.02	4.2	0.87	1.00	0.02	4.2	0.99	1.02	0.02	4.2	1.12	0.95	0.02
C11	3.5	0.45	1.05	0.02	3.5	0.53	1.08	0.02	3.5	0.62	1.06	0.02	3.5	0.73	0.99	0.02
C12	3.5	0.54	1.04	0.02	3.5	0.65	1.05	0.01	3.5	0.73	1.07	0.02	3.5	0.84	1.03	0.02
C13	7.8	-0.33	1.22	0.09	4.7	-0.29	1.15	0.07	3.1	-0.39	1.46	0.06	-	-	-	-
C14	4.4	0.17	1.09	0.02	4.4	0.26	1.10	0.02	4.4	0.35	1.06	0.02	4.4	0.42	1.10	0.03
C15	5.3	0.18	1.07	0.02	5.3	0.24	1.12	0.02	5.3	0.36	1.06	0.02	5.3	0.39	1.13	0.03

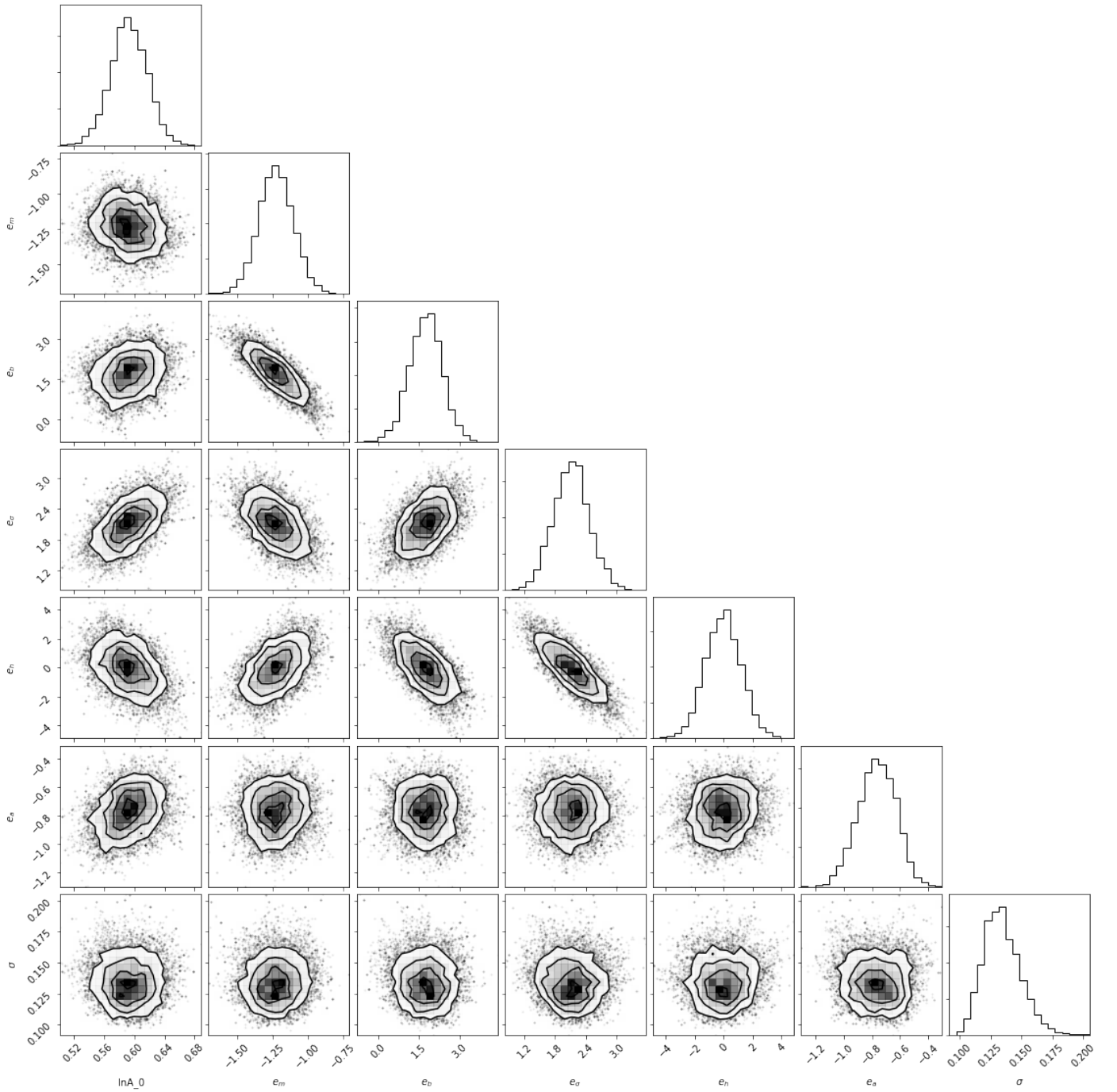


Fig. B.1. Posterior associated to Likelihood that minimises to Eq 7. $\ln A_0$ is the normalisation ($0.64^{+0.03}_{-0.03}$ in Eq. 7), σ is the gaussian-scatter of the fit, and $e_m, e_b, e_\sigma, e_h, e_a$ are, respectively, the exponents for logarithm of $\Omega_m, \Omega_b, \sigma_8, h_0, 1/(1+z)$ divided by the respective pivot as discussed in Sec. 3.2.